Yipin Su[1]
Sonny Astani Department of Civil and Environmental Engineering,
University of Southern California,
Los Angeles, CA 90089
e-mail: su_yp@zju.edu.cn

An Xin
Sonny Astani Department of Civil and Environmental Engineering,
University of Southern California,
Los Angeles, CA 90089
e-mail: axin@usc.edu

Qiming Wang[1]
Sonny Astani Department of Civil and Environmental Engineering,
University of Southern California,
Los Angeles, CA 90089
e-mail: qimingw@usc.edu

Mechanics of Living Lattice Composites With Growing Crystals

Lattice composites show excellent mechanical and acoustic properties. Compared with traditional man-made lattice composites, natural (or living) lattice composites exhibit the ability to spontaneously increase their stiffness as time increases, i.e., self-enhancement. With this paper, we study the mechanism of the self-enhancement behavior of living lattice composites. We first immerse a polymeric lattice in an oversaturated $CaCO_3$ solution to simulate the self-enhancement behavior of living lattice composites. We then propose a modeling framework to quantitatively describe the evolution of the morphology and effective stiffness of the growing composites, including a phase field model simulation, a crystal growth prediction, and a modified lattice mechanics theory. We validate the modeling work through comparison among the theoretical prediction, experimental observation, and finite element simulation. We also study the effects of the cross sections of polymeric beams, initial concentration of the solution, and architecture type on the self-enhancement behavior of the composites. This paradigm is expected to open promising avenues for the design and fabrication of synthetic living lattice composites. [DOI: 10.1115/1.4056581]

Keywords: self-enhancement, phase field model, modified lattice mechanics theory, effective stiffness, mechanical properties of materials, stress analysis, structures

1 Introduction

Lattice composites are periodic structures made up of struts that exhibit wide applications in aerospace, aircraft, civil engineering, military, and bioengineering [1–4]. They can be manufactured at length scales ranging from millimeters to centimeters through some well-established industrial processes, such as interlacing [5], molding hot-press [6], filament winding [7], cutting method [8], weaving [9], interlocking [10], and additive manufacturing [11]. Compared with traditional materials and structures, lattice composites present many advantages, including lightweight, good thermal diffusivity, and high toughness [4,12,13], thus have attracted considerable attention from academia and industry alike.

Inevitably, there is a risk of failure resulting from manufacturing defects and in-service damage accumulation in the working process of lattice composites, which pose clear limitations on their applications [14,15]. Designing and fabricating lattice composites with tunable properties to optimally meet the operational requirements of devices at different stages is eagerly pursued by engineers. In this aspect, the nature mother provides us with lightening inspirations.

Natural living lattice composites such as woods, bones, and insect wings are mimicked in many modern technical composites, including honeycombs and foams [16–18]. One of the most attractive characteristics of these natural lattice bio-composites is that they can enhance themselves gradually by increasing their stiffness and strength as time increases, i.e., the self-enhancement behavior assisted by the living cells [19]. However, traditional man-made composites are usually fabricated with permanent configurations and constituents and hence with irrevocable physical properties. Self-enhanced behavior of natural living composites is not presented in traditional man-made structures.

So far, some research has been proposed for the study of lattice composites. For example, in a recent review paper [20], the definition, classification, application, and fabricating methods of lattice structures are concluded. Fan and Yang [21] developed an equivalent continuum method to analyze the effective stiffness of three-dimensional stretching-dominated lattice materials. Hawreliak et al. [22] performed dynamic compression experiments to study the emergence of behavior owing to the lattice periodicity in additive manufacturing materials on length scales that approach a single unit cell. Song et al. [23] adopted three-dimensional (3D) printing and electroless plating techniques to uniformly deposited nickel film on the surface of prestine polymer lattices to obtain metal-coated meso-lattice composites. Wang et al. [24] conducted a preliminary investigation of pyramidal lattice truss-core sandwich structures fabricated from carbon fiber-reinforced composites. Li et al. [25] designed and fabricated a novel carbon fiber-reinforced corrugated lattice truss-core sandwich cylinder (LTSC) to get a strong, stiff, and weight-efficient cylindrical shell. Frulloni et al. [26] presented a finite element modeling of the failure behavior of lattice composite hollow structures subjected to external hydrostatic pressure. Morozov et al. [27] investigated the buckling behavior of anisogrid composite lattice cylindrical shells under axial compression, transverse bending, pure bending, and torsion. However, the study of the self-enhanced behavior of living lattice composites is, however, still a blank. A systematical investigation of mechanics of living lattice composites is highly desired to completely understand the structures and harvest their full potential.

Mathematically, some advanced theories have been developed to model the evolution of the morphology of living tissues and plants in nature, including the swelling theory of hydrogel [28,29] and growth theory [30,31]. However, these theories have some deficiencies. For example, most of the studies based on these theories took the assumption that the studied objectives are isotropic and homogeneous. Besides, these theories can well capture the evolution of the shape and volume of the elastomer but cannot describe the

[1]Corresponding authors.

Contributed by the Applied Mechanics Division of ASME for publication in the Journal of Applied Mechanics. Manuscript received October 7, 2022; final manuscript received December 19, 2022; published online January 23, 2023. Assoc. Editor: Yuhang Hu.

variation of the elastic properties such as shear modulus and stiffness of the material during the growth. Most of the existing modeling studies were focused on elastomers with simplified regular shapes such as plates, tubes, and spheres. It is still an open question how to model the evolution of the morphology and elastic properties of growing living lattice composites.

Here, we propose an approach to mimic the self-enhancement of living lattice composites via bacteria-assisted crystal precipitation within a polymeric lattice composite immersed in an oversaturated solution. The initial polymer scaffold is prepared via the 3D-printing technology [32–36], which has been widely adopted in many areas to manufacture complex 3D structures. We propose a crystal growth theory to theoretically capture the evolution procedure. A phase field model [37,38] simulating the crystal growth of the composite in the oversaturated $CaCO_3$ medium is employed to validate this theoretical model. We should note that the growth model proposed here is microscopic and generally anisotropic. To simplify the simulation, we adopt the isotropic growth assumption. A good agreement between experimental observation and numerical simulation is obtained. The effective stiffness of the resulting two-phase lattice composite is calculated through an energy-equivalent method [39]. Good agreements among theoretical modeling, experimental investigation, and finite element (FE) simulation are achieved, which verify the reliability and accuracy of the study. Our work is expected to advance the mechanics of self-strengthened lattice bio-composites and provide a solid reference for the design and fabrication of novel bionic materials and devices.

The paper is structured as follows. In Sec. 2, we present the experimental procedures and results for the bacteria-assisted precipitation of a polymeric lattice composite immersed in an oversaturated $CaCO_3$ solution. Modeling framework is then constructed in Sec. 3, including the phase field model for bacteria-assisted precipitation, the crystal growth theory governing the evolution of the thickness of the growing crystal layer, the modified lattice mechanics theory for the calculation of the effective stiffness of the resulting lattice composite, and the finite element simulation of the effective Young's modulus of the two-phase composite. In Sec. 4, we compare the theoretical, experimental, and FE results. We also study the influences of factors such as the shape of the beam cross section, initial concentration of the $CaCO_3$ solution, and architecture type on the effective stiffness of the growing composite. Finally, we draw some conclusions in Sec. 5.

2 Experimental

Here, we describe our experimental method, with results presented in Fig. 1.

Formlabs tough resin, a commercial 3D-printable material, was purchased from Formlabs. Dimethylacetamide (DMA), phenylbis (2,4,6- trimethylbenzoyl) phosphine oxide (photo initiator), Sudan I (photo absorber), and ethanol were purchased from Sigma-Aldrich. Sodium hydroxide and hydrochloric acid were purchased from GR ACS. Sporosarcina pasteurii (ATCC 11859, non-infectious) was purchased from ATCC (American Type Culture Collection). To prepare ATCC 1832 and the precipitation medium, tryptone, ammonium sulfate, ammonium chloride, sodium bicarbonate, and calcium chloride were purchased from Sigma-Aldrich. Urea, tricine, yeast extract, agar, and L-glutamic acid were purchased from Alfa Aesar. Difco nutrient broth was purchased from Fisher Scientific. All chemicals were directly used without further purification.

To prepare the photocurable polymer resin, 6 g tough resin was first dissolved into 3 g DMA solvent and mixed well by stirring for around 1 h. Thereafter, 0.09 g photoinitiator and 0.01 g Sudan I were added into the solution and stirred for another 1 h until fully dissolved. The additive manufacturing of lattice structures was performed with a projection-based stereolithography (SLA) system, which has been described before [40]. A computer-aided-design (CAD) model of a lattice structure was first designed and sliced into an image sequence. Subsequently, these images were sequentially projected with blue light (405 nm) onto a liquid basin. The liquid resin in the basin was then solidified by light exposure, forming a solid layer bonded onto the printing stage. As the printing stage was lifted up, the fresh resin refluxed beneath the printing stage. By lowering down the stage to a prescribed height and illuminating the resin with another slice image, a second layer was printed and bonded onto the first layer. The aforementioned procedure was repeated several times; each layer was set as 28 μm thickness and the polymerization process required 14 s. Subsequently, the 3D-printed lattice structures were washed with pure ethanol and dried in air at 70 °C for 24 h to evaporate the DMA solvent.

BPU medium (ATCC 1832 medium) containing 10 g/L tryptone, 5 g/L yeast extract, 4.5 g/L tricine, 5 g/L ammonium sulfate, 2 g/L glutamic acid, and 10 g/L urea was adjusted to pH 8.6 ± 0.1 using NaOH solution (1 M), and then filter-sterilized with a 0.2-μm autoclaved filter. Agar aqueous solution (15 g/L) was autoclaved separately and added into the aforementioned medium to obtain a solid medium for bacteria growth and proliferation. The urea–$CaCl_2$ medium contains 3 g/L Difco nutrient broth, 20 g/L urea, 10 g/L ammonium chloride, and 2.12 g/L sodium bicarbonate. pH value was adjusted with HCl solution (1 M) to below 6.0; then, the medium was autoclaved at 121 °C and 21 psi for 45 min; 28 g $CaCl_2$ was dissolved into this cooled, sterilized solution as the precipitation medium. All glassware was autoclaved at 121 °C and 21 psxi for 15 min before use.

The bacteria (*S. pasteurii*) were inoculated and proliferated on the prepared solid medium for two days at 30 °C. After then, the bacteria were transferred into the BPU medium to grow for another 24 h at 30 °C. To induce the bio-mineralization process, the polymer lattice samples were soaked in 150 mL BPU medium with bacteria for 24 h at 30 °C. Subsequently, the samples were immersed in 150 mL $CaCl_2$–urea medium in an incubator at 28 °C, 50 rpm. The precipitation medium was refreshed manually every day. These samples were taken out after 10 days, washed with 70% alcohol solutions, and then annealed on a hot plate at 70 °C for 24 h. As a result, the 3D-printed polymer scaffolds were transformed into lattice composites with biologically induced $CaCO_3$.

3 The Modeling Framework

In this section, we construct a framework to understand the mechanism of self-enhancement of a growing 3D polymeric lattice structure. First, we employ a phase field model to quantitatively simulate a lattice structure immersed in an oversaturated $CaCO_3$ solution. Second, we derive the evolution law of thickness of the growing crystal layer. Then, we develop a modified method to calculate the effective stiffness of the growing two-phase lattice composite. Finally, we implement a finite element method (FEM) to simulate the effective stiffness of the lattice composite numerically.

3.1 Phase Field Model for Crystal Growth. The movement and attachment of the solute atoms to the solid–liquid interface results in the precipitation phenomenon, which can be described by a phase field model, as illustrated in Fig. 2. This method is based on the idea that the Helmholtz free energy of the system is given by [41,42]

$$F(\phi, c) = \int_{\Omega} \left[f(\phi, c) + \frac{1}{2}\varepsilon^2 (\nabla\phi)^2 + \frac{1}{2} k_c (\nabla c)^2 \right] d\Omega \qquad (1)$$

where Ω is the region occupied by the system, $f(\phi, c)$ is the Helmholtz free energy density for a uniform phase with no gradient, ϕ is the phase field, with $\phi = 0$ corresponding to the liquid phase of $CaCO_3$ solution and $\phi = 1$ the solid phase, c is the concentration of the solution, ε is a small constant which determines the thickness of the interface of the two phases, and k_c is the interfacial coefficient; ∇ is the gradient operator, which in the 3D Cartesian corrdinate system $(x \quad y \quad z)$ is given by $\nabla = \left(\partial/\partial x \quad \partial/\partial y \quad \partial/\partial z\right)^T$. The energy contributions $\varepsilon^2(\nabla\phi)^2/2$ and $k_c(\nabla c)^2/2$ in Eq. (1) are

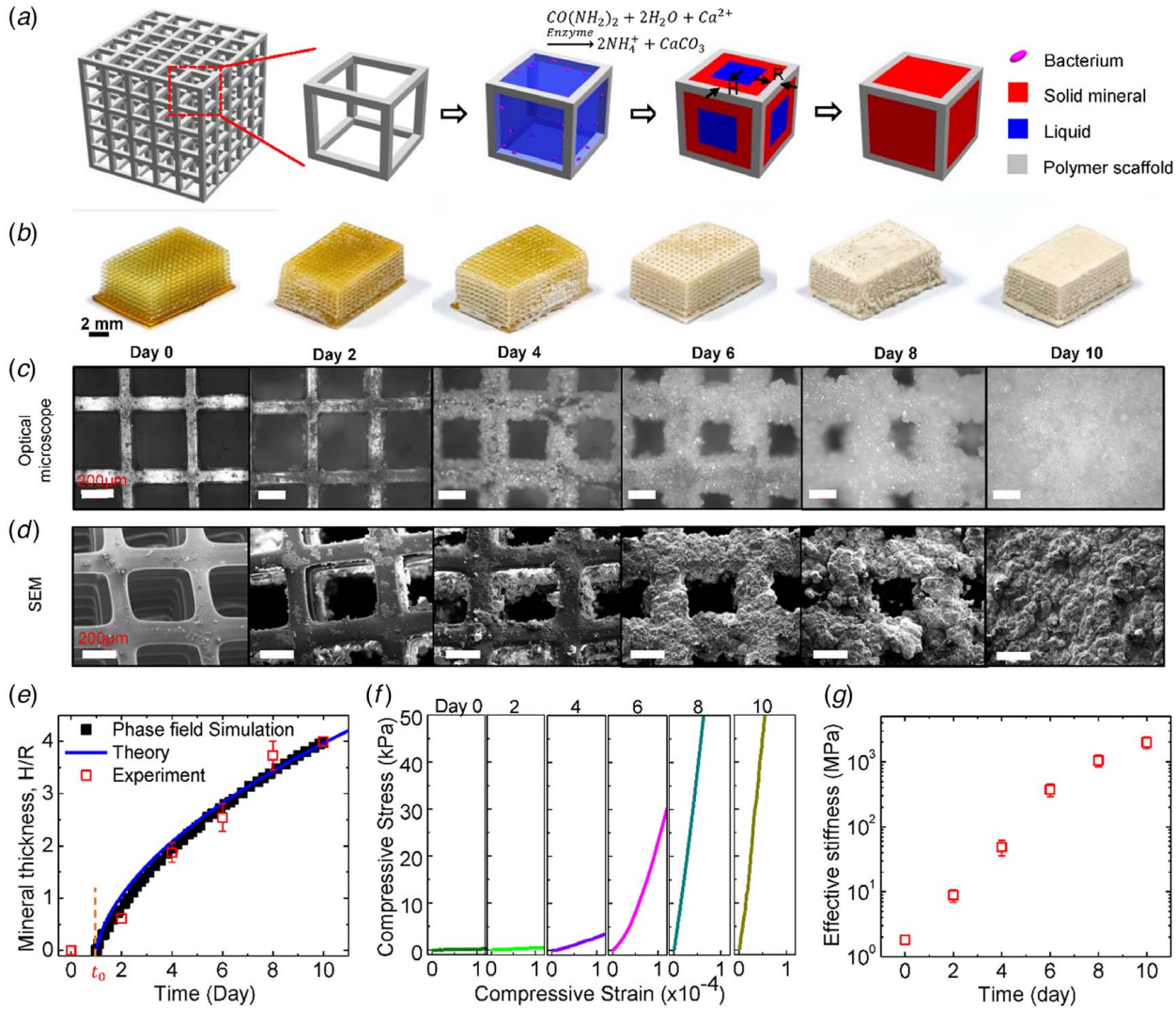

Fig. 1 Bacteria-assisted mineral growth within a lattice scaffold: (*a*) schematics to show the bacterial-assisted mineral growth process. *H* is the mineral thickness and *R* is the half beam width, (*b*) samples and their, (*c*) optical microscopic images and (*d*) scanning electronic microscopic images during the bacteria-assisted mineral growth process over 10 days, (*e*) experimentally observed, phase-field simulated, and theoretically calculated normalized mineral thickness in functions of time, (*f*) the relationships between compressive stress and strain of the mineralized sample over 10 days, and (*g*) Young's modulus of the mineralized sample over 10 days. The error bars are standard deviations of 3–5 tests.

due to the gradients in the phase and concentration fields, respectively.

The non-conserved phase field variable ϕ and the conserved concentration-field variable c are functions of position x and time t. According to non-equilibrium thermodynamics [38,41–43], the equations governing the evolution of the fields take the form

$$\tau\frac{\partial\phi}{\partial t} = -\frac{\delta F}{\delta\phi} \tag{2}$$

$$\frac{\partial c}{\partial t} = \nabla M\nabla\frac{\delta F}{\delta c} \tag{3}$$

where τ is a positive characteristic time reflecting the interfacial movement from the ordered phase to the disordered one and M is related to the atomic mobility of the solute [38]. Both M and τ are taken to be constants in this calculation.

Here, we adopt a specific normalized double-well energy density with the form [41]

$$f(\phi, c) = \frac{A_1}{2c_0^2}(c-c_1)^2 + \frac{A_2}{2c_0}(c_2-c)\phi^2 - \frac{A_3}{3}\phi^3 + \frac{A_3}{4}\phi^4 \tag{4}$$

where $A_1 = 238.4$, $A_2 = 58$, $A_3 = 21.14$ are nondimensional constants, $c_1 = 0.288$ (mol/L) is a constant concentration, $c_2 = 0.6$ (mol/L) is the concentration of $CaCO_3$ within the solid precipitation [40], and $c_0 = 2.56$ (mol/L) is a constant concentration for nondimensionalization.

Then, the differential Eqs. (3) and (4) can be written as

$$\tau\frac{\partial\phi}{\partial t} = \varepsilon^2\nabla^2\phi - \frac{\partial f}{\partial\phi} \tag{5}$$

$$\frac{\partial c}{\partial t} = M\left(-k_c\nabla^2\nabla^2 c + \frac{\partial f}{\partial c}\right) \tag{6}$$

where $\nabla^2 = \partial^2/\partial x^2 + \partial^2/\partial y^2 + \partial^2/\partial z^2$ is the Laplace operator in the three-dimensional Cartesian corrdinate system.

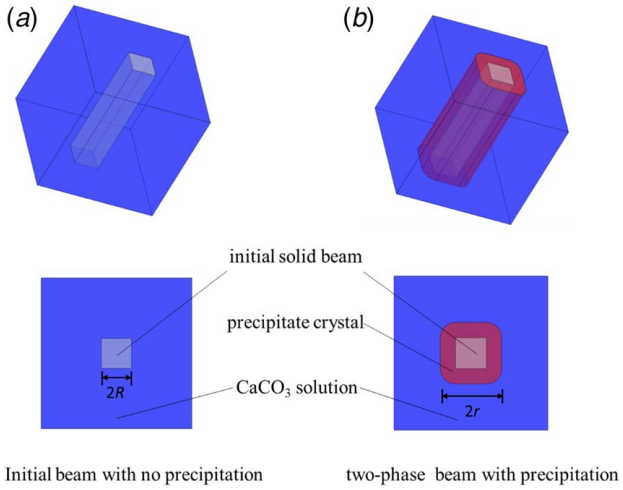

Fig. 2 Phase-field model for the crystal growth procedure of a solid beam immersed in an oversaturated $CaCO_3$ solution, (*a*) a square beam is first immersed in an oversaturated $CaCO_3$ solution, (*b*) then $CaCO_3$ crystal precipitates from the solution as time goes on and adheres to the surface of the beam, resulting in a growing two-phase composite. The geometric dimensions of the initial beam and the growing composite beam are 2*R* and 2*r*, respectively. The upper row presents the three-dimensional images of the growth procedure and the lower row shows the two-dimensional counterparts.

We now nondimensionalize the governing equations by introducing the following nondimensional quantities

$$\bar{\tau}=\frac{D}{A_1 l^2}\tau,\quad \bar{t}=\frac{D}{A_1 l^2}t,\quad \bar{\varepsilon}=\frac{\varepsilon}{l},\quad \bar{c}=\frac{c}{c_0},\quad \bar{k}_c=\frac{k_c c_0^2}{l^2}$$
$$\bar{M}=\frac{MA_1}{c_0^2 D},\quad \bar{\nabla}=\left(\frac{\partial}{\partial\bar{x}}\quad\frac{\partial}{\partial\bar{y}}\right)^T=\nabla l,\quad \bar{x}=\frac{x}{l},\quad \bar{y}=\frac{y}{l} \tag{7}$$

where D is the diffusivity of the solute and l is a representative length of the system Ω.

Then, Eqs. (5) and (6) read

$$\bar{\tau}\frac{\partial\phi}{\partial t}=\bar{\varepsilon}^2\bar{\nabla}^2\phi-A_4\phi^3-A_3\phi^2-A_2(\bar{c}_2-\bar{c})\phi \tag{8}$$

and

$$\frac{\partial\bar{c}}{\partial t}=\bar{M}\left(-\bar{k}_c\bar{\nabla}^2\bar{\nabla}^2\bar{c}+\frac{A_1}{2}\bar{\nabla}^2\bar{c}-\frac{A_2}{2}\bar{\nabla}^2\phi^2\right) \tag{9}$$

respectively.

The boundary condition of the problem is $\frac{\partial\phi}{\partial n}=\frac{\partial c}{\partial n}=0$, where n is the outward normal to the boundary. It means that there is no change in the total composition of the system due to transport across its boundary.

Next, we define the initial conditions for the problem. The initial concentrations of the $CaCO_3$ precipitate and the solution are set as $c_2=0.6$ mol/L and $c_m=0.25$ mol/L, respectively. As a result, $CaCO_3$ crystals precipitate in the oversaturated solution and attach to the solid beam, resulting in crystallite growth [40].

Finally, the evolution of the system can be obtained by solving Eqs. (8) and (9). In the following, we solve these highly coupled equations in the general form partial differential equation (PDE) module in COMSOL MULTIPHYSICS 5.4.

3.2 Crystal Growth Theory. In an oversaturated $CaCO_3$ solution with initial concentration c_m, the atoms move to the interface and attach to the surface of the beam (with initial radius R). The crystal gradually grows together to cover the beam and form a precipitate layer with radius r at time t, as depicted in Fig. 3. As a result, the solid–liquid interface moves to the locate r with an instantaneous velocity $v=dr/dt$.

The solution far away from the precipitate interface is assumed to make no contribution to the precipitation, thus its concentration remains unchanged as $c_m(=0.251$ mol/L according to our calculation). The concentration of the solute within the solid precipitation is c_p. The solute atoms are absorbed to the interface for the formation of the precipitation layer. As a result, the closer the solution is to the precipitate front, the smaller its concentration will be. The solution adjacent to the interface has the equilibrium (saturated) concentration c_e (≈ 0.00012991 mol/L in pure water at room temperature). Therefore, we adopt the assumption $c_e \ll c_p, c_m$.

For the unit area of the interface to advance a distance dr within a time interval dt, the number of $CaCO_3$ atoms must be supplied from the liquid phase to the solid phase by diffusion is [42]

$$dN=(c_p-c_e)dr \tag{10}$$

According to Fick's first law [44], the flux of atoms through a unit area in time interval dt is

$$dN=D\frac{\partial c}{\partial r}dt \tag{11}$$

where D is the diffusion coefficient of $CaCO_3$ atoms within the solution, r is the distance from the center of the lattice beam, and $c(r, t)$ is the instantaneous concentration of the solution at time t and position r.

Equating Eqs. (10) and (11) yields [40,42]

$$\frac{dr}{dt}=\frac{D}{c_p-c_e}\frac{dc}{dr} \tag{12}$$

Following a simplified approach originally proposed by Zener

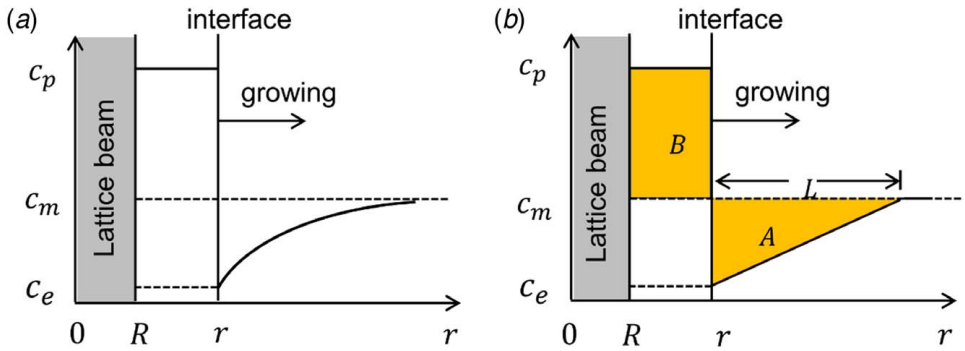

Fig. 3 Diffusion model for the crystal growth procedure: (*a*) concentration profile of the system and (*b*) simplification of the concentration profile

[45], we assume that the concentration of the solution varies linearly from c_e to c_m along the distance of L at the front of the mineral, as depicted in Fig. 3(*b*). Thus, the concentration gradient can be approximated as

$$\frac{dc}{dr} = \frac{c_m - c_e}{L} \tag{13}$$

The conservation of solute requires that the numbers in the two shaded areas A and B along the unit length in Fig. 3(*b*) be equal, i.e.

$$\pi(r^2 - R^2)(c_p - c_m) = \pi[(r+L)^2 - r^2]\left(\frac{c_m - c_e}{2}\right) \tag{14}$$

We thus obtain L as

$$L = \sqrt{r^2 \frac{2c_p - c_m - c_e}{c_m - c_e} - R^2 \frac{2c_p - 2c_m}{c_m - c_e}} - r \tag{15}$$

From Eqs. (12)–(15), we have

$$\frac{dr}{dt} = \frac{D(c_m - c_e)}{(c_p - c_e)\left(\sqrt{r^2 \frac{2c_p - c_m - c_e}{c_m - c_e} - R^2 \frac{2c_p - 2c_m}{c_m - c_e}} - r\right)} \tag{16}$$

Since $c_e << c_m < c_p$, we rewrite Eq. (16) as

$$\frac{dr}{dt} = \frac{Dc_m}{c_p\left(\sqrt{r^2 \frac{2c_p - c_m}{c_m} - R^2 \frac{2c_p - 2c_m}{c_m}} - r\right)} \tag{17}$$

Writing the mineral thickness as $H = r - R$, Eq. (17) can be rewritten as

$$\frac{d(H/R)}{d(Dt/R^2)} = \frac{1}{\frac{c_p}{c_m}\sqrt{(H/R+1)^2\left(\frac{2c_p}{c_m} - 1\right) - \left(\frac{2c_p}{c_m} - 2\right)} - H/R - 1} \tag{18}$$

The initial condition is $H(t=0) = 0$. We set $c_p/c_m = \alpha$, $H/R = Y$, and $Dt/R^2 = X$; then, Eq. (18) can be further simplified as

$$\left[\alpha\sqrt{(Y+1)^2(2\alpha - 1) - (2\alpha - 2)} - Y - 1\right]dY = dX \tag{19}$$

Integrating Eq. (19) from $X = 0$ to X, we obtain

$$\frac{\alpha(\alpha-1)}{\sqrt{2\alpha-1}}\left\{\left[(Y+1)\sqrt{\frac{2\alpha-1}{2\alpha-2}}\sqrt{\frac{2\alpha-1}{2\alpha-2}(Y+1)^2 - 1} - \ln\left(\sqrt{\frac{2\alpha-1}{2\alpha-2}(Y+1)^2 - 1} + (Y1)\sqrt{\frac{2\alpha-1}{2\alpha-2}}\right)\right] - \left[\frac{\sqrt{2\alpha-1}}{2\alpha-2} - \ln\left(\sqrt{\frac{1}{2\alpha-2}} + \sqrt{\frac{2\alpha-1}{2\alpha-2}}\right)\right]\right\}$$
$$-\frac{Y^2}{2} - Y = X \tag{20}$$

In general, the normalized mineral thickness can be written as a function of time t as

$$H/R = G(Dt/R^2, \alpha) \tag{21}$$

where $G()$ is a function, which can be determined from Eq. (20).

3.3 Lattice Mechanics Theory

3.3.1 Energy-Equivalent Method. Consider a unit cell of the two-phase lattice composite as shown in Fig. 4, with the beams composed of two isotropic linear elastic materials. Here and thereafter, the initial solid beam and the growing precipitation layer are denoted as phases "*s*" and "*p*," respectively, with the associated physical parameters indicated with the superscripts "*s*" and "*p*." According to the constitutive equation of linear isotropic elasticity, the strain of the kth ($k = s, p$) phase can be expressed as

$$\varepsilon_{ij}^k = \frac{1}{E^k}[\sigma_{ij}^k(1 + \nu^k) - \nu^k \delta_{ij}\sigma_{qq}^k], \quad (i, j = x, y, z) \tag{22}$$

where $\varepsilon_{ij}^k = \varepsilon_{ji}^k$ and $\sigma_{ij}^k = \sigma_{ji}^k$ are the strain and stress components of the solid, respectively, E^k is Young's modulus and ν^k is Poisson's ratio of the material, and δ_{ij} is the Kronecker Delta. Note that the Einstein summation convention of summing on repeated indices is used.

We equivalent the two-phase cell to a homogeneous cube composed of a single linear phase with an unkonwn elastic constant.

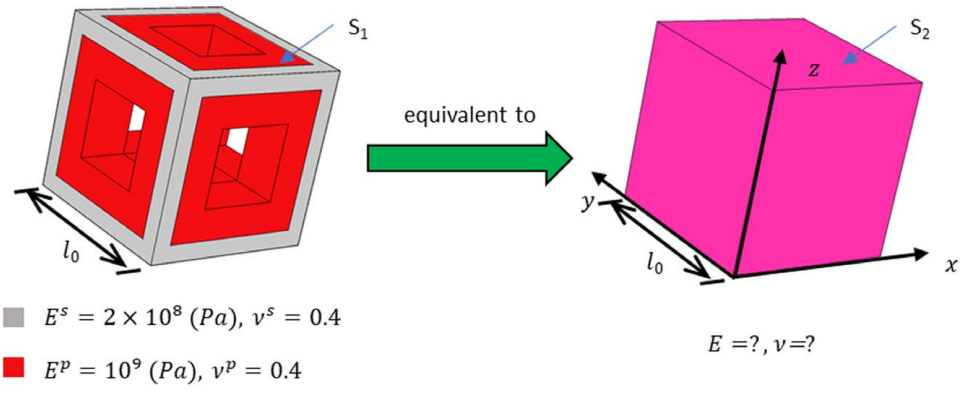

Fig. 4 Representative topology of a cellular two-phase lattice composite (left) and its homogeneous equivalent (right). The Young's modulus and Poisson's ratio of the initial polymeric beam are $E^s = 2 \times 10^8$ and $\nu^s = 0.4$, respectively, and the Young's modulus and Poisson's ratio of the $CaCO_3$ are $E^p = 10^9$ and $\nu^p = 0.4$, respectively. S_1 is the area of the top face of the two-phase cellular lattice and $S_2 = l_0^2$ is the area of the top face of the equivalent homogeneous cubic, with l_0 being the length of beams of the two cubic cells.

The idea to calculate the effective elastic properties of the equivalent cubic cell is that an identical strain imposed on the top faces of the two cells should result in the same strain energy [39].

For the two-phase lattice cell (left in Fig. 4), we first consider a *uniaxial macroscopic strain* applied along the z-direction on the top face, $\varepsilon_{zz} = \varepsilon$, with all other components of the imposed stress being zero. In this case, we assume that only the four beams of the cell along the z-direction deform and others remain undeformed. The kth phase in each deformed beam experiences uniform principal strains and stresses given by

$$\sigma_{xx}^k = 0, \quad \sigma_{yy}^k = 0, \quad \varepsilon_{zz}^k = \varepsilon \tag{23}$$

From Eqs. (22) and (23), we determine the other principal stress and strain components as

$$\varepsilon_{xx}^k = \varepsilon_{yy}^k = -\nu^k \varepsilon, \quad \sigma_{zz}^k = E^k \varepsilon \tag{24}$$

Using Eqs. (23) and (24), the strain energy of the kth phase with volume V^k of the two-phase unit cell is

$$W_u^k = \frac{1}{2}(\sigma_{xx}^k \varepsilon_{xx}^k + \sigma_{yy}^k \varepsilon_{yy}^k + \sigma_{zz}^k \varepsilon_{zz}^k)\frac{1}{3}V^k = \frac{E^k \varepsilon^2}{6} V^k \tag{25}$$

As a result, the total energy of the two-phase unit cell due to the uniaxial macroscopic strain is

$$W_u = \frac{E^s \varepsilon^2}{6} V^s + \frac{E^p \varepsilon^2}{6} V^p \tag{26}$$

Next, we consider a *pure dilatation* of the unit cell with a volumetric strain ε_V. Then, we have $\varepsilon_{xx} = \varepsilon_{yy} = \varepsilon_{zz} = \varepsilon_V/3$. In this case, all the 12 beams of the cell deform identically. We consider the beams along the z-direction, for example; then the uniform principal strains and stresses of the kth phase in these beams are given by

$$\sigma_{xx}^k = 0, \quad \sigma_{yy}^k = 0, \quad \varepsilon_{zz}^k = \varepsilon_V/3 \tag{27}$$

The other principal stress and strain components can be obtained by solving Eqs. (22) and (27) as

$$\varepsilon_{xx}^k = \varepsilon_{yy}^k = -\frac{\nu^k \varepsilon_V}{3}, \quad \sigma_{zz}^k = \frac{E^k \varepsilon_V}{3} \tag{28}$$

Using Eqs. (27) and (28), the strain energy of the kth phase with volume V^k of the two-phase unit cell is

$$W_d^k = \frac{1}{2}(\sigma_{xx}^k \varepsilon_{xx}^k + \sigma_{yy}^k \varepsilon_{yy}^k + \sigma_{zz}^k \varepsilon_{zz}^k)V^k = \frac{E^k \varepsilon_V^2}{18} V^k \tag{29}$$

As a result, the total elastic energy of the two-phase unit cell due to the pure dilation is

$$W_d = \frac{E^s \varepsilon_V^2}{18} V^s + \frac{E^p \varepsilon_V^2}{18} V^p \tag{30}$$

At last, we consider a *simple shear* of the two-phase cell, with macroscopic strains

$$\varepsilon_{xy} = \varepsilon_{yx} = \frac{\gamma}{2} \tag{31}$$

where γ is the shear amount.

In this case, only the four beams of the two-phase cell along the z-direction deform, with the strains of the kth phase given by

$$\varepsilon_{xy}^k = \varepsilon_{yx}^k = \frac{\gamma}{2} \tag{32}$$

Solving Eqs. (22) and (32) yields the non-zero stress components as

$$\sigma_{xy}^k = \sigma_{yx}^k = \frac{E^k}{1+\nu^k}\frac{\gamma}{2} \tag{33}$$

Then, the energy of the kth phase in the two-phase cell reads

$$W_\gamma^k = \frac{1}{2}(\sigma_{xy}^k \varepsilon_{xy}^k + \sigma_{yx}^k \varepsilon_{yx}^k)\frac{1}{3}V^k = \frac{E^k}{1+\nu^k}\frac{\gamma^2}{12}V^k \tag{34}$$

As a result, the total elastic energy of the two-phase unit cell due to the simple shear is

$$W_\gamma = \frac{E^s}{1+\nu^s}\frac{\gamma^2}{12}V^s + \frac{E^p}{1+\nu^p}\frac{\gamma^2}{12}V^p \tag{35}$$

Now, we consider the equivalent homogeneous cell (right in Fig. 4). It has a cubic symmetry thus its elastic law reads

$$\begin{bmatrix} \sigma_{xx} \\ \sigma_{yy} \\ \sigma_{zz} \\ \sigma_{yz} \\ \sigma_{xz} \\ \sigma_{xy} \end{bmatrix} = \begin{bmatrix} C_{11} & C_{12} & C_{12} & 0 & 0 & 0 \\ C_{12} & C_{11} & C_{12} & 0 & 0 & 0 \\ C_{12} & C_{12} & C_{11} & 0 & 0 & 0 \\ 0 & 0 & 0 & C_{44} & 0 & 0 \\ 0 & 0 & 0 & 0 & C_{44} & 0 \\ 0 & 0 & 0 & 0 & 0 & C_{44} \end{bmatrix} \begin{bmatrix} \varepsilon_{xx} \\ \varepsilon_{yy} \\ \varepsilon_{zz} \\ 2\varepsilon_{yz} \\ 2\varepsilon_{xz} \\ 2\varepsilon_{xy} \end{bmatrix} \tag{36}$$

where C_{ij} is the component of the elasticity matrix.

Subject to a uniaxial strain with $\varepsilon_{zz} = \varepsilon$ and other strain components zero, the strain energy of the equivalent cell with single phase reads

$$\bar{W}_u = \frac{1}{2} V C_{11} \varepsilon^2 \tag{37}$$

and equals to the result in Eq. (26) for the two-phase unit cell. Here

$$V = l_0^3 \tag{38}$$

is the volume of the equivalent unit cell.

The strain energy of the equivalent cell subject to a pure dilatation with $\varepsilon_{xx} = \varepsilon_{yy} = \varepsilon_{zz} = \varepsilon_V/3$ and other strain components zero is

$$\bar{W}_d = \frac{1}{6} V (C_{11} + 2C_{12}) \varepsilon_V^2 \tag{39}$$

and equals to the result in Eq. (30).

For the equivalent cell subject to a simple shear with $\varepsilon_{xy} = \varepsilon_{yx} = \gamma/2$ and other strain components zero, the strain energy is

$$\bar{W}_\gamma = \frac{1}{2} V C_{44} \gamma^2 \tag{40}$$

and equals the result in Eq. (35).

In total, we have the following relations

$$\begin{aligned} \frac{E^s \varepsilon^2}{6} V^s + \frac{E^p \varepsilon^2}{6} V^p &= \frac{1}{2} V C_{11} \varepsilon^2 \\ \frac{E^s \varepsilon_V^2}{18} V^s + \frac{E^p \varepsilon_V^2}{18} V^p &= \frac{1}{6} V (C_{11} + 2C_{12}) \varepsilon_V^2 \\ \frac{E^s}{1+\nu^s}\frac{\gamma^2}{12} V^s + \frac{E^p}{1+\nu^p}\frac{\gamma^2}{12} V^p &= \frac{1}{2} V C_{44} \gamma^2 \end{aligned} \tag{41}$$

Then, the moduli of the equivalent homogeneous cubic cell can be obtained from Eq. (41) as

$$\begin{aligned} C_{11} &= \frac{E^s V^s + E^p V^p}{3V}, \quad C_{12} = 0, \\ C_{44} &= \frac{E^s V^s (1+\nu^p) + E^p V^p (1+\nu^s)}{6(1+\nu^s)(1+\nu^p)V} \end{aligned} \tag{42}$$

Note here that we have $C_{12} = 0$, which means there is no overall Poisson effect in the equivalent cubic cell. This can happen in a usual equivalent material [46].

Then, the overall Young modulus of the equivalent cubic cell can be derived as

$$E = \frac{(C_{11} - C_{12})(C_{11} + 2C_{12})}{C_{11}} = \frac{E^s V^s + E^p V^p}{3V} \tag{43}$$

3.3.2 Modified Energy-Equivalent Method. We note that the derivation of the formula (43) is based on the assumption that the beams of the composite cell are thin. In this section, we extend the energy-equivalent method to the case of thick-beam lattices.

For lattices with thick beams, Eq. (25) should be modified as

$$W_u^k = \frac{1}{2}(\sigma_{xx}^k \varepsilon_{xx}^k + \sigma_{yy}^k \varepsilon_{yy}^k + \sigma_{zz}^k \varepsilon_{zz}^k) t^k V^k = \frac{t^k E^k \varepsilon^2}{2} V^k \tag{44}$$

where t^k ($k = s, p$) is the volume ratio of the stressed region to the total region of the kth phase.

Then, Eq. (26) reads

$$W_u = \frac{t^s E^s \varepsilon^2}{2} V^s + \frac{t^p E^p \varepsilon^2}{2} V^p \tag{45}$$

For the unit cubic cell undergoes pure dilatation, the stress and strain distributed homogeneously in all the beams of the structure; thus, Eq. (30) always holds, which is independent of the thickness of the beams.

Then, Eq. $(41)_{1,2}$ should be rewritten as

$$\begin{aligned} \frac{t^s E^s \varepsilon^2}{2} V^s + \frac{t^p E^p \varepsilon^2}{2} V^p &= \frac{1}{2} V C_{11} \varepsilon^2 \\ \frac{E^s \varepsilon_V^2}{18} V^s + \frac{E^p \varepsilon_V^2}{18} V^p &= \frac{1}{6} V (C_{11} + 2C_{12}) \varepsilon_V^2 \end{aligned} \tag{46}$$

Finally, the modified effective Young's modulus of the cubic lattice can be derived from Eq. (46) as

$$\begin{aligned} E &= \frac{(C_{11} - C_{12})(C_{11} + 2C_{12})}{C_{11}} \\ &= \frac{(E^s V^s + E^p V^p)[E^p V^p (9t^p - 1) + E^s V^s (9t^s - 1)]}{18V(t^s E^s V^s + t^P E^p V^p)} \end{aligned} \tag{47}$$

Consider a two-phase cubic cell with beam length l_0, initial beam thickness R and precipitated beam thickness H. When subject to a uniaxial strain, stress occurs in four of 12 beams of the structure, with the stressed region shown in Fig. 5. The total volume of the initial solid beam is

$$V^s = 4R^2 l_0 + 8R^2(l_0 - 2R) \tag{48}$$

The volume of the stressed part of the initial solid frame is

$$V^s_{strain} = 4R^2 l_0 \tag{49}$$

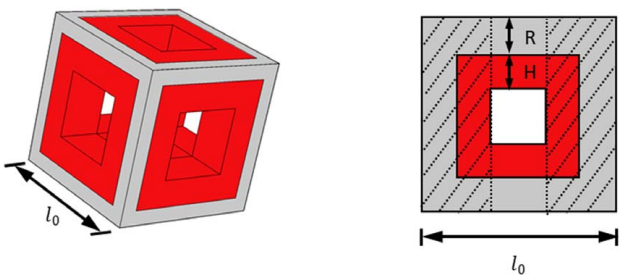

Fig. 5 3D schematic diagram of a cubic cell with two phases (left) and its 2D front view (right). The shadow represents the stressed region of the structure when subject to a uniaxial strain

The total volume of the precipitated beamexperimental results are marked is

$$V^p = 4(R + H)^2 l_0 + 8(R + H)^2(l_0 - 2R - 2H) - V^s \tag{50}$$

The volume of the stressed part of the precipitated beam is

$$V^p_{strain} = V^p - 8(l_0 - 2R - 2H)[(R + H)^2 - R^2] \tag{51}$$

Then, the volume ratio of each phase in Eq. (47) can be determined once the initial structure parameters are given, as

$$t^s = \frac{V^s_{strain}}{V^s}, \quad t^p = \frac{V^p_{strain}}{V^p} \tag{52}$$

The effective Young's modulus of the cubic lattice can be obtained using Eq. (47). For the case that the beams are thin sufficiently, we have $t^s = t^p = 1/3$. Then, Eq. (47) reduces to the formulation (43).

3.4 Finite Element Simulation of the Effective Young's Modulus. In this section, we illustrate the finite element method for the calculation of the effective Young's modulus of the two-phase cubic cell.

The shear modulus and Poisson's ratio of the initial polymeric beam are taken to be $E^s = 2 \times 10^8$ and $\nu^s = 0.4$, respectively, and those parameters of the $CaCO_3$ precipitation layer be $E^p = 10^9$ and $\nu^p = 0.4$, respectively. We carry out the simulations using a finite element package, COMSOL Multiphysics 5.4 for the two-phase cubic cell subject to a uniform small displacement u_z at the top face, with the planes parallel to the z-direction being traction free, i.e., $\sigma_{xx} = \sigma_{yy} = 0$. The corresponding average stress applied at the top face of the cell is measured as $\bar{\sigma}_{zz}$.

Then according to the relationship

$$\varepsilon_{zz} = \frac{1}{E}[\sigma_{zz} - \nu(\sigma_{xx} + \sigma_{yy})] \tag{53}$$

the overall Young's modulus of the equivalent cubic cell can be obtained as

$$E = \frac{\sigma_{zz}}{\varepsilon_{zz}} \tag{54}$$

where $\varepsilon_{zz} = u_z / l_0$ is the strain along the z-direction of the equivalent cell, and $\sigma_{zz} = \bar{\sigma}_{zz} \times S_1 / S_2$ is the average stress applied at the top face of the equivalent cubic cell, with S_1 and S_2 being the areas of the top faces of the two-phase and equivalent homogeneous cubic cells, respectively.

4 Results and Discussion

In this section, we present the numerical results of the phase field simulation for crystal growth and lattice mechanics for evolution of the morphology, volume, and effective stiffness of the growing two-phase lattice composite. We will first present the results of two-dimensional phase field simulation for crystal growth which compared with three-dimensional simulation are easy to calculate due to the less degree-of-freedom of the problem. The aim of these calculations is twofold: first, to verify the accuracy of the phase field model for crystal growth by comparing the experimental results in Fig. 1 with theoretical prediction from formula (21), and second, to quantitatively determine the nondimensional parameters (Eq. (7)) of the phase field model for this problem. With the determined parameters, calculation for three-dimensional crystal growth will then be presented. The molar concentration of $CaCO_3$ within the solid precipitation and the initial concentration of the oversaturated $CaCO_3$ solution are taken to be $c_p = 0.6$ mol/L and $c_m = 0.25$ mol/L, respectively, if not state otherwise. All the modeling

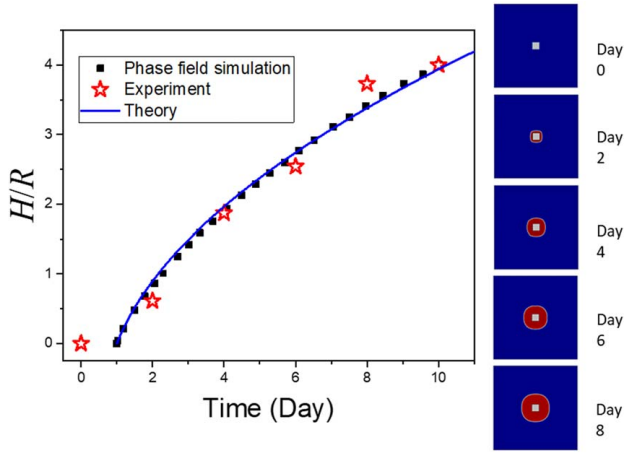

Fig. 6 Experimental, theoretical and phase field modeling results of two-dimensional crystal growth for different days: (left) plot of the incremental thickness of the precipitate as a function of time and (right) instantaneous 2D morphology features of cross section of the two-phase composite beam at day 0, 2, 4, 6, and 8. The experimental results are marked with stars.

results will be verified through comparison with those of experiments and FEM simulations.

During the calculation, we use

$$\bar{\tau} = 8.5 \times 10^{-4}, \quad D = 5 \times 10^{-13}, \quad l = 10^{-4}, \quad \bar{M} = 1, \quad \bar{k}_c = 10^{-3}, \quad \bar{\varepsilon} = 0.055 \tag{55}$$

4.1 Results for Crystal Growth. Figure 6 presents the comparison between two-dimensional phase field simulation for crystal growth, theoretical modeling, and experimental results. Note that the theoretical result is obtained for beams with circular cross section, while the experiment and phase field simulation are for beams with square cross sections. We can see that the influence of the geometry can be approximately ignored. The thickness of the crystal layer is measured form Fig. 1. Note that the mineral precipitation is governed by bacteria attached to the polymer beam and the corresponding enzyme secretion; therefore, the bacteria attachment and growth process are not instantaneous and a certain period of t_0 is required to initiate the mineral growth and the mineral growth starts at $t_0 =$ day 1. It can be observed that a $CaCO_3$ crystal layer grows gradually around the initial beam due to precipitation as time increases, keeping an approximately square cross section.

According to the growth theory presented in Sec. 3.2, the thickness of a growing crystal evolves according to the law (21). Using the experimental parameter $R = 50\ \mu$m and estimated parameters $\alpha = 4.8$, $D = 5 \times 10^{-13}\ m^2/s$, we can obtain the relationship between H/R and mineralization growth time, plotted in Fig. 6. Good agreement among the theoretical prediction, experimental observation and phase field simulation is achieved, verifying the accuracy and rationality of the phase field model and the crystal growth theory.

In Fig. 7, phase field results for crystal growth of beams with different cross-section shapes immersed in an oversaturated $CaCO_3$ solution are examined to study the effect of the beam cross section on the morphology evolution. Here, six beam cross sections with a fixed initial area S_0 are considered, including triangle, square, pentagon, hexagon, and circle. We can see that the area of the growing crystal layer ΔS increases almost linearly over time, which is independent of the shape of the beam. Note that the beam grows into a tube gradually as the radius of the cross section increases. In particular, it can be observed that the beam with a triangular cross section grows fastest in its area, followed by the beams with square, pentagonal, pentagonal, and circular cross sections. The physical mechanism behind this phenomenon can be understood as follows. With the same area, the triangle has the longest perimeter compared with the other shapes. The longer perimeter guarantees a larger contact area between the beam and the $CaCO_3$ solution and more attached crystals; thus, a larger area increase. Based on this mechanism, the enhancement of the growing lattice composite can be optimized by finitely designing the shape of the cross section of the beams.

With the parameters from 2D simulations, we present the result of 3D phase field modeling in Fig. 8. Due to symmetry, we study a single cubic cell of the 3D lattice composite in Fig. 1, containing oversaturated $CaCO_3$ solution inside. As time goes on, a two-phase composite is formed, with the $CaCO_3$ crystal layer precipitates and attaches to the initial solid beam, resulting in an increase of the total volume of the two solid phases. After 8 days' crystal growth, the volume of the initial structure can be increased more than seven times. Note that the growth saturation happens after day 9 and the

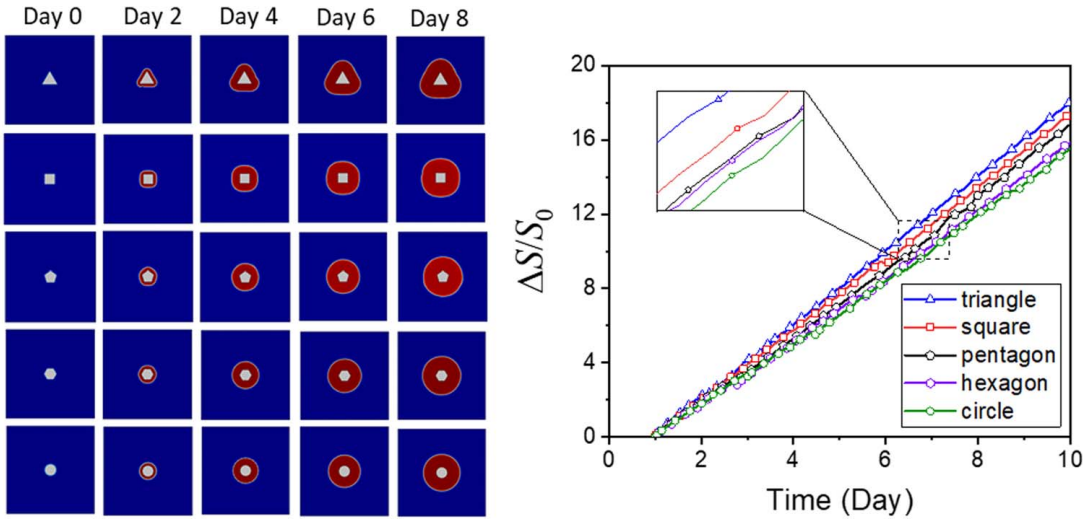

Fig. 7 Effect of the shape of the cross section of the initial solid beam on the evolution of the incremental $CaCO_3$ precipitation layer as a function of time: (left) instantaneous 2D morphology features of triangular, square, pentagonal, pentagonal, and circular beams at days 0, 2, 4, 6, and 8 and (right) plot of the incremental area of the cross section of the growing two-phase beam as a function of time.

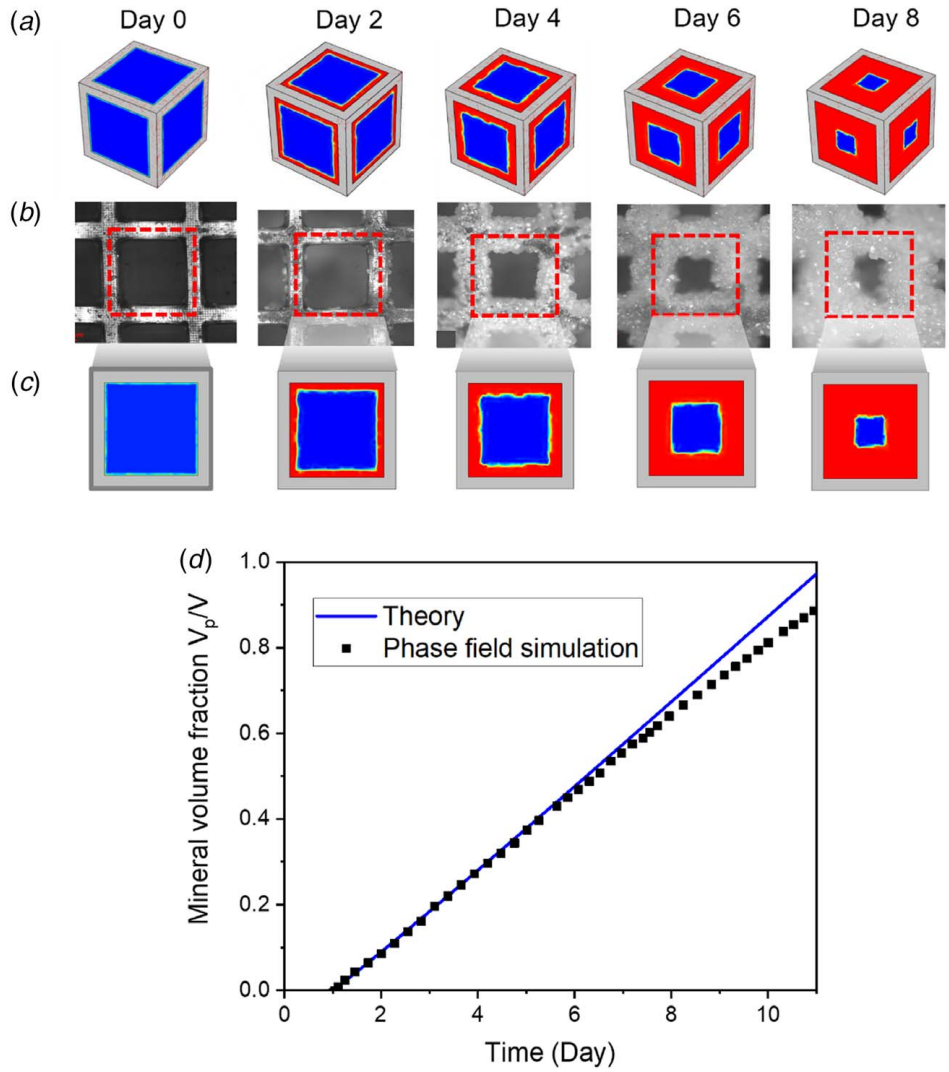

Fig. 8 3D phase-field simulation of a lattice composite cell immersed in an oversaturated C_aCO_3 solution: (*a*) 3D instantaneous morphology features of the growing cell using the phase-field modeling at day 0, 2, 4, 6, and 8, (*b*) 2D view of the experimental images, (c) 2D instantaneous morphology features of the growing cell using the phase field modeling, and (*d*) theoretical predication and phase field simulation on variation of the incremental volume of the crystal layer as a function time

void of the lattice will be filled with $CaCO_3$ crystal, which is noted presented here. Using the theoretical result in Fig. 6, we can obtain the growing volume of the composite. Once the thickness of the precipitation layer is obtained, the total volume of the growing crystal can be approximated using Eq. (50). Figure 8(*d*) presents the variation of the volume ratio V^p/V as the function of the growing time. Our theoretical model predicts a linear increase of the crystal volume as the growing time increases. The phase field modeling result indicates that the volume of the crystal increases linearly with time at first, agreeing well with the theoretical prediction. However, the growth rate of the crystal decreases eventually as time increases further, which can be ascribed to the decrease in the concentration of the $CaCO_3$ solution. The volume obtained by the phase field simulation deviates from that by the theoretical prediction after day 6, which seems to contradict the results shown in Fig. 6. That is because in our theory, we assume that the cross section of the growing beam remains square. While the cross section of the growth is not exactly a square as the time increase (the right panel in Fig. 6). It can be expected that the crystal will stop growing and the 3D shape of the composite will be fixed when the concentration of the solution reaches the equilibrium value c_e. Hence, the lattice composite can be enhanced on demand by tuning the initial concentration of the solution, which will be studied in the following.

4.2 Results for Lattice Mechanics. In Fig. 9, we verify the accuracy of the theoretical model (Eq. (43)) and the modified theoretical model (Eq. (47)) for the overall stiffness of the growing two-phase lattice composite. Here, we use the same geometry for theoretical model and FEM simulation, i.e., the ideal geometry as presented in Fig. 5. The initial volume ratio of the solid frame is set as $V^s/V = 10\%$. We can see that the formation of the $CaCO_3$ precipitation layer around the initial solid beam can greatly enhance the stiffness of the lattice composite. The effective stiffness of the composite increases as the crystal grows. The theoretical prediction agrees well with the FEM simulation when the volume of the growing crystal is small, while it deviates from the FEM result when the volume of the crystal becomes large because our theoretical model (Eq. (43)) is only applicable to the lattice composite with thin beams. It can be seen that the modified theoretical model (Eq.(47)) we established presents a better prediction result, especially for the case of thick-beam composites.

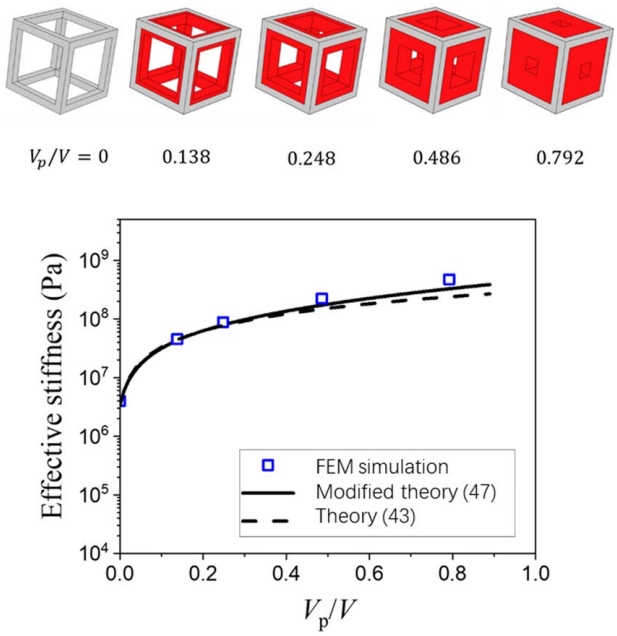

Fig. 9 Comparison between the theoretical, modified theoretical, and FEM results of the effective stiffness of the two-phase lattice composite with varying volume. The upper row presents the 3D images of the cell structures with $V^p/V = 0$, 0.118, 0.248, 0.426, 0.621, 0.792, and the lower row displays the plot of the effective stiffness of the two-phase cell as a function of volume ratio V^p/V. The FEM results corresponding to the specific structures in the upper row are marked with square points

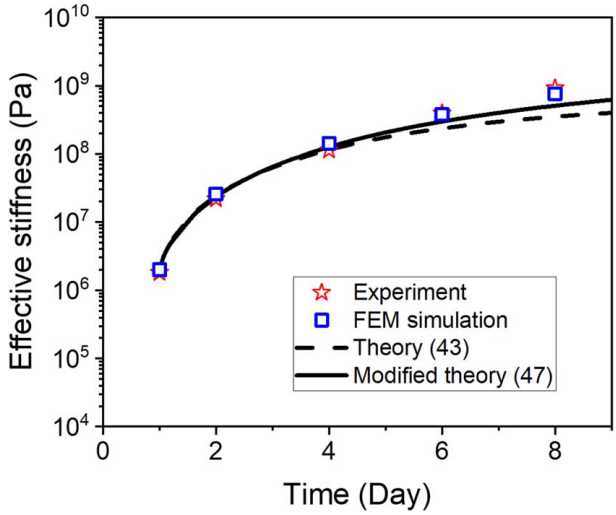

Fig. 10 Effective stiffness of a growing two-phase lattice composite: comparison among theory, modified theory, FEM simulation, and experimental result

4.3 Results for Living Composite Lattices. Once the theoretical model (Eq.(43)) and modified theoretical model (Eq.(47)) are verified, we use them to predict the overall stiffness of the growing lattice composite, with the results presented in Fig. 10. Good agreements are achieved among theoretical prediction, modified theoretical result, FEM simulation, and experimental observation, verifying the accuracy of modeling work for the overall stiffness of the growing lattice composite. It can be seen that after 8 days' precipitate accumulation, the magnitude of the stiffness of the resulting two-phase composite is about two orders larger than that of the initial polymer lattice structure.

Figure 11 displays the influence of the volume fraction of the initial solid frame on the effective stiffness of the growing lattice composite. The calculation stops when the cubic cell is almost filled by $CaCO_3$ precipitate crystal. We can see that composite composed of beams with a lower initial volume fraction take more time to fill the hollow structure. The initial effective stiffness of the

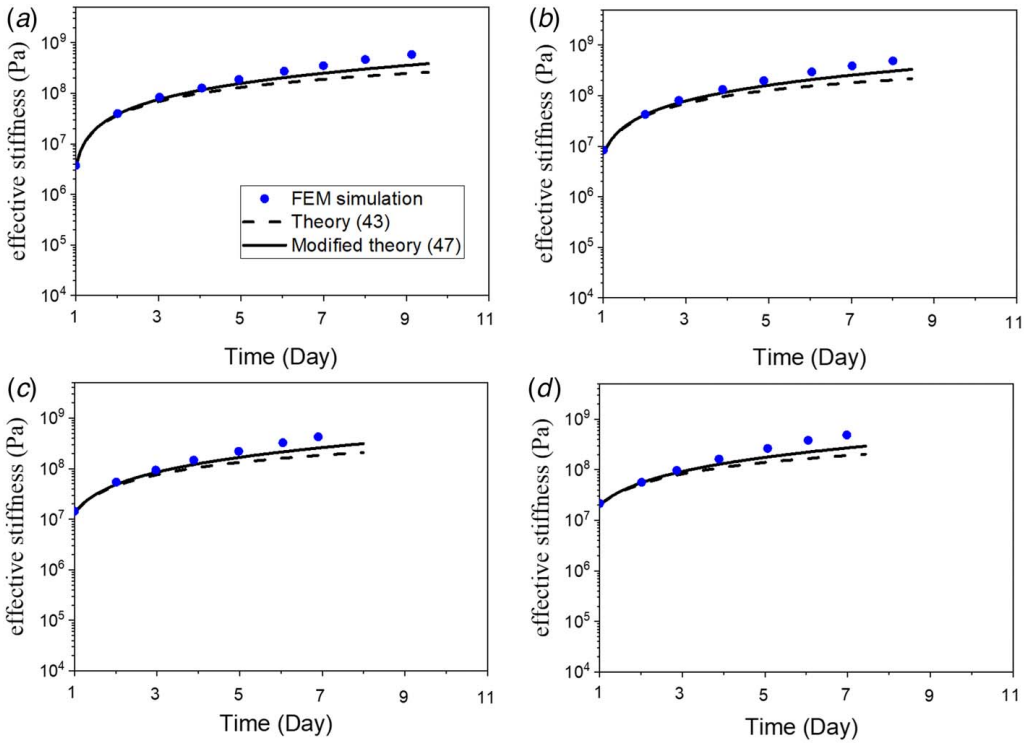

Fig. 11 Effective stiffness of the growing lattice composites with the initial volume fraction of the solid beam V^s/V being: (*a*) 5%, (*b*) 10%, (c) 20%, and (*d*) 30%, respectively

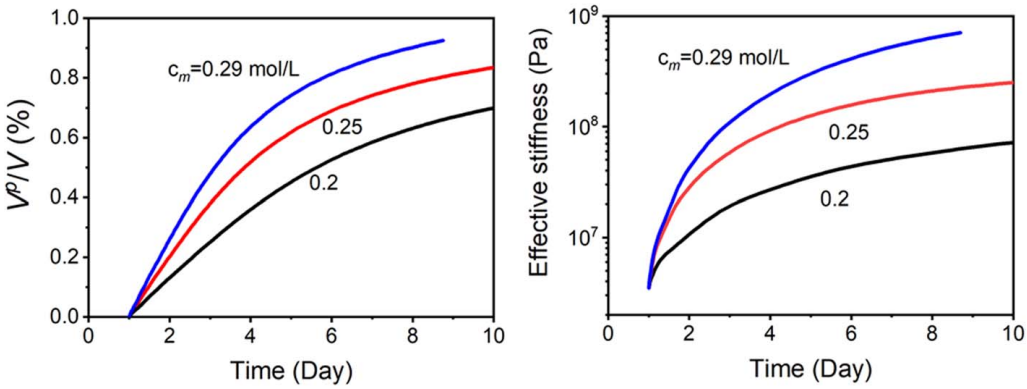

Fig. 12 Effect of the initial concentration of the $CaCO_3$ solution c_m on the evolution of the (left) incremental volume ratio V^p/V and (right) effective stiffness of the growing lattice composite

composite composed of beams with a higher volume fraction is larger than that of the composite composed of beams with a lower volume fraction, but the stiffness of the latter structure has a larger tunable range.

In Fig. 12, we investigate the evolution of the volume and effective stiffness of a solid polymeric lattice composite with an initial volume ratio $V^s/V = 10\%$ immersed in an oversaturated $CaCO_3$ solution with varying concentration $c_m = 0.16,\ 0.2,\ 0.25$ mol/L. Here, we just present the result of the modified theoretical model. Obviously, the lattice in the solution with a higher concentration grows faster than that in the solution with a lower concentration, which indicates that the mechanical behavior of the growing composite can be tailored by designing the initial concentration of the $CaCO_3$ solution.

Using Eqs. (47) and (A.13), we present in Fig. 13 the comparison of the evolution of the volume and effective stiffness of the cubic, octet, and octahedral lattice composites. The initial volume ratio

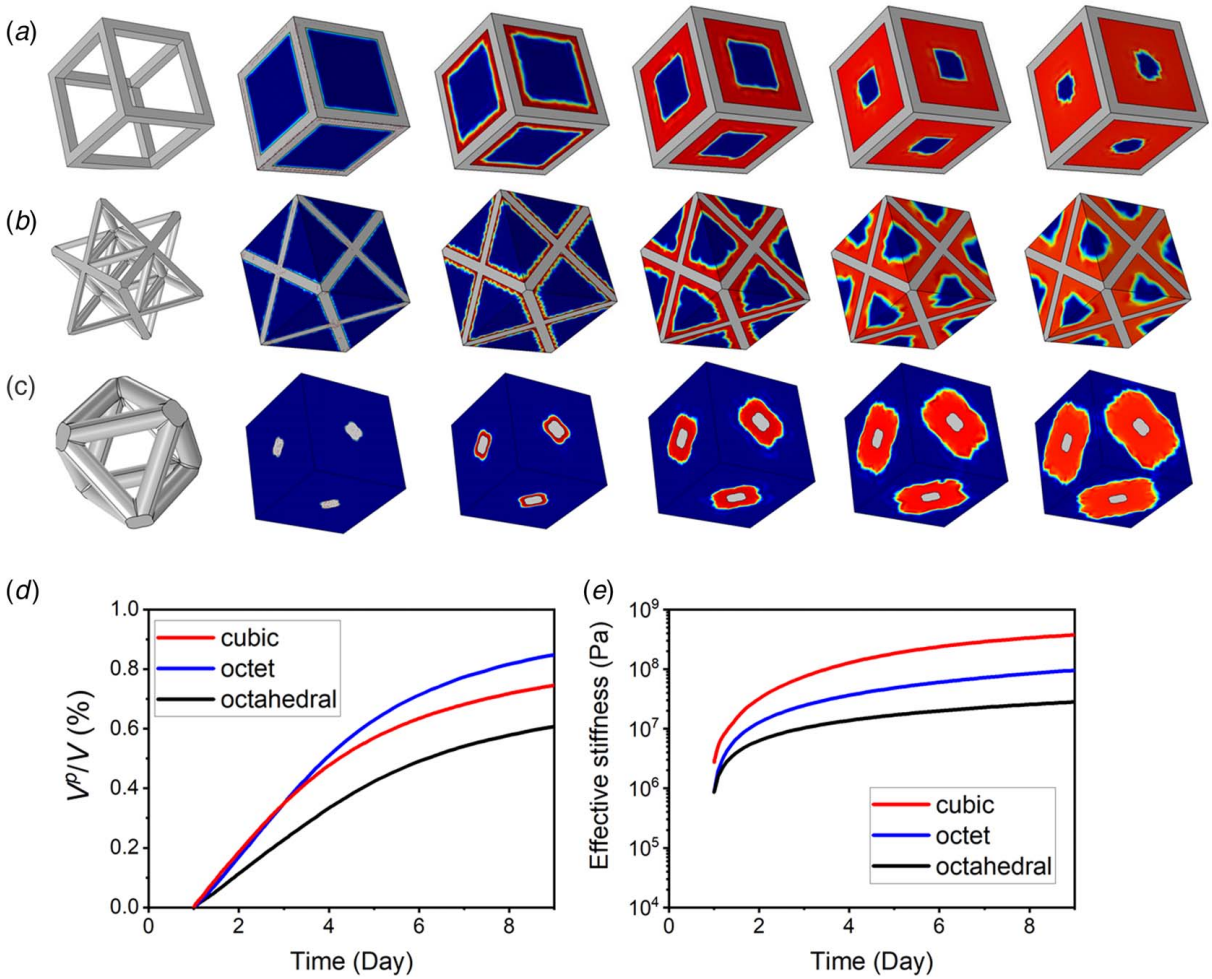

Fig. 13 Effect of architecture type of the cell: (*a*) cubic, (*b*) octet, and (c) octahedral on the evolution of the (*d*) volume ratio V^p/V and the (*e*) effective stiffness of the growing two-phase lattice composites

of the polymeric frame of the three structures is fixed as $V^s/V = 10\%$. It can be seen that the octet lattice increases fastest in volume, while the cubic lattice increases fastest in effective stiffness. Note that the effective stiffnesses of octet and octahedral composites with identical V^p/V are the same, because the effective stiffness of the two structures follows the same law (A.13). While the effective stiffness of the octet lattice is always larger than the one of the octahedral lattice, because the larger crystal volume increase as shown in Fig. 13(*d*). This result may render strong guidance for optimizing the mechanical behavior of living lattice composites.

5 Conclusive Remarks

In conclusion, we construct a modeling framework to explain the self-enhancement behavior of growing lattice composites. We employ a phase field model to quantitatively describe a polymeric lattice composite immersed in an oversaturated $CaCO_3$ solution. Compared with the growth and swelling theories, the phase field method can well describe the morphological evolution of the composites and the resulting governing equations are easier to solve. Whereas our phase field model is restricted in several ways and can be improved upon. For example, in our model, the atomic mobility of the solute is assumed to be a constant in each phase. In fact, the solute diffusivity in the solid is about four orders of magnitude smaller than that in the liquid [47]. This restriction could be overcome in the future by allowing the quantity M to depend on ϕ and c [38,48]. We also assume an isotropic crystal growth to simplify the calculation. Anisotropy can be introduced by assuming that ε depends on the direction of the outer normal vector $\mathbf{n} = -\nabla\,\phi$ at the interface, i.e., $\varepsilon = \varepsilon(\mathbf{n})$ [38].

We develop a modified lattice mechanics theory to obtain the effective stiffness of the resulting two-phase composite lattice, based on the energy-equivalent method. Note here that the two phases of the composite are assumed to be linear elastic materials. Non-linear elasticity should be employed for soft materials [49]. In addition, this method is only applicable to composite lattice with thin beams. More accurate analysis of stress and strain is required for structures with thick beams.

To validate the phase field model and the modified lattice mechanics theory, we also derive theoretically the evolution law of the thickness of the precipitation layer starting from the diffusion theory and implement a finite element model to numerically simulate the effective stiffness of the growing lattice composite. Despite the assumptions we adopt, good agreement among the phase field modeling, experimental observation, and FEM simulation is achieved, indicating the validity and accuracy of the study. Results show that the geometry and effective stiffness of the growing composite can be designed on demand by finely tuning the cross section of the beam, the initial concentration of the solution, and the architecture type. We expect that our model can provide a solid reference for the design and fabrication of novel bionic functional devices.

Acknowledgment

Q.W. acknowledges funding support from the Office of Naval Research (Grant No. N00014-22-1-2019) and the National Science Foundation (Grant Nos. CMMI-1943598, FMRG-2229228, and DBI-2222206).

Conflict of Interest

There are no conflicts of interest.

Data Availability Statement

The authors attest that all data for this study are included in the paper.

Appendix: Effective Stiffnesses of Octet and Octahedral Trusses

Here we derive the effective stiffnesses of octet and octahedral trusses as shown in Fig. 14. From Eqs. (37), (39), (43), and (47), we can see that the effective stiffness of material with cubic symmetry can be determined from analysis of the uniaxial strain and pure dilatation deformations. Note that the stress and strain states in the octet and octahedral trusses subject to uniaxial strain and dilatation are completely identical; thus, their effective stiffnesses are the same. In the following, we consider the two composites together.

Energy-Equivalent Method. For unit cells of the octet and octahedral trusses, consider first a uniaxial macroscopic strain imposed in the x_3 direction, with the only non-zero strain component being $\varepsilon_{zz} = \varepsilon$. The kth phase in each deformed beam experiences uniform principal strains and stresses given by

$$\sigma_I^k = 0, \quad \sigma_{II}^k = 0, \quad \varepsilon_{III}^k = \frac{\varepsilon}{2} \tag{A1}$$

where *I*, *II*, and *III* are the orthometric principal directions of each beam. The strains and stresses of the beam satisfy the relationship

$$\varepsilon_{ij}^k = \frac{1}{E^k}[\sigma_{ij}^k(1+\nu^k) - \nu^k\delta_{ij}\sigma_{qq}^k] \ \ (i,j = I,\ II,\ III) \tag{A2}$$

where $\varepsilon_{ij}^k = \varepsilon_{ji}^k$ and $\sigma_{ij}^k = \sigma_{ji}^k$ are the strain and stress components of the solid, respectively, E^k is Young's modulus and ν^k is Poisson's ratio of the material, and δ_{ij} is the Kronecker Delta. Note that the Einstein summation convention of summing on repeated indices is adopted.

Then, the other principal stress and strain components of each deformed beam can be obtained from Eqs. (A1) and (A2) as

$$\varepsilon_I^k = \varepsilon_{II}^k = -\frac{\nu^k\varepsilon}{2}, \quad \sigma_{III}^k = \frac{E^k\varepsilon}{2} \tag{A3}$$

Using Eqs. (A1) and (A3), we obtain the strain energy of the kth phase with volume V^k of the two-phase unit cells as

$$W_u^k = \frac{1}{2}(\sigma_I^k\varepsilon_I^k + \sigma_{II}^k\varepsilon_{II}^k + \sigma_{III}^k\varepsilon_{III}^k)\frac{2}{3}V^k = \frac{E^k\varepsilon^2}{12}V^k \tag{A4}$$

As a result, the total energy of the two-phase unit cells due to the uniaxial macroscopic strain is

$$W_u = \frac{E^s\varepsilon^2}{12}V^s + \frac{E^p\varepsilon^2}{12}V^p \tag{A5}$$

Next, we consider pure dilatation of the unit cell with a volumetric strain ε_V. In this case, all beams of the cell deform identically. The principal strain and stress components in the beams are

$$\begin{aligned} &\sigma_I^k = 0, \quad \sigma_{II}^k = 0, \quad \varepsilon_{III}^k = \frac{\varepsilon_V}{3} \\ &\varepsilon_I^k = \varepsilon_{II}^k = -\frac{\nu^k\varepsilon_V}{3}, \quad \sigma_{III}^k = \frac{E^k\varepsilon_V}{3} \end{aligned} \tag{A6}$$

Then, the strain energy of the kth phase with volume V^k of the two-phase unit cell can be obtained from Eq. (A6) as

$$W_d^k = \frac{1}{2}(\sigma_I^k\varepsilon_I^k + \sigma_{II}^k\varepsilon_{II}^k + \sigma_{III}^k\varepsilon_{III}^k)V^k = \frac{E^k\varepsilon_V^2}{18}V^k \tag{A7}$$

As a result, the total elastic energy of the two-phase unit cells due

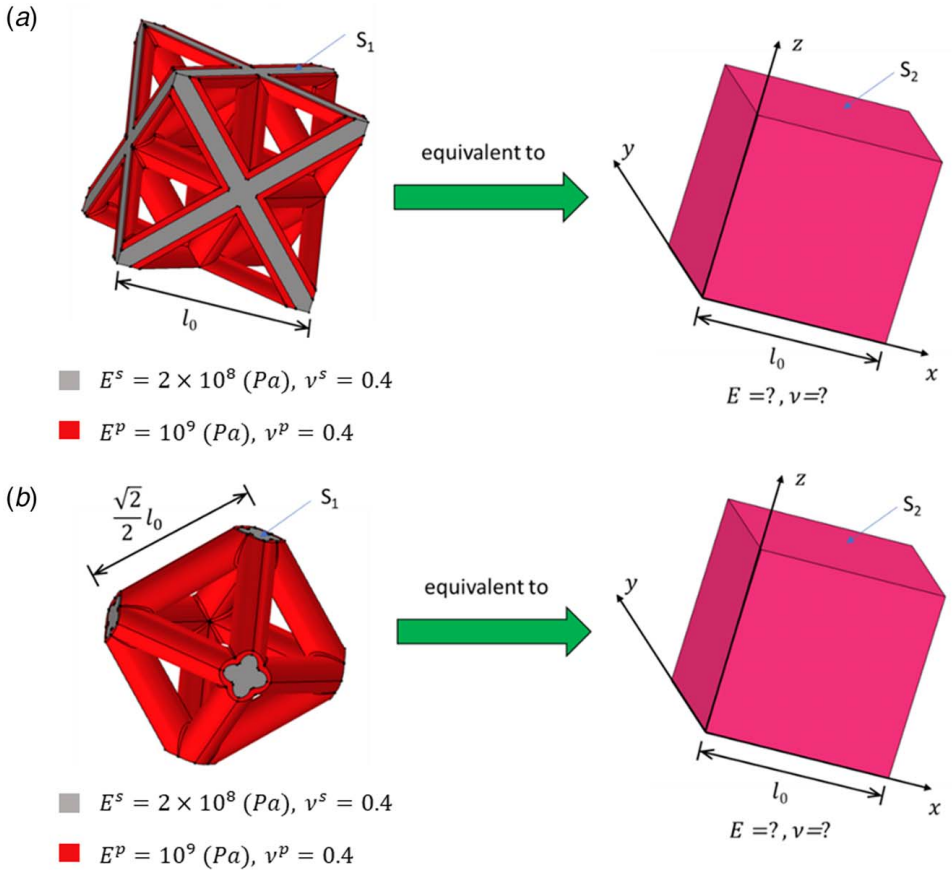

Fig. 14 Representative topology of a cellular two-phase lattice cell (left) and its homogeneous equivalent (right): (*a*) octet cell and (*b*) octahedral cell. The Young's modulus and Poisson's ratio of the initial polymeric beam are $E^s = 2\times10^8$ and $\nu^s = 0.4$, respectively, and the Young's modulus and Poisson's ratio of the $CaCO_3$ are $E^p = 10^9$ and $\nu^p = 0.4$, respectively, S_1 is the area of the top face of the two-phase cellular lattice and $S_2 = l_0^2$ is the area of the top face of the equivalent homogeneous cubic. l_0 is the length of beams of the two equivalent cubic cells.

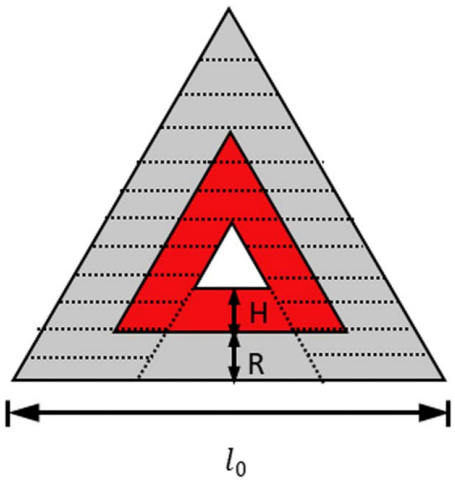

Fig. 15 A 2D sectional view of tetrahedron unit of octet and octahedral lattices. The length, initial beam thickness and precipitated beam thickness are l_0, R, and H, respectively. The shadow represents the stressed region of the structure when subject to a uniaxial strain

to the pure dilation is

$$W_d = \frac{E^s\varepsilon_V^2}{18}V^s + \frac{E^p\varepsilon_V^2}{18}V^p \tag{A8}$$

Similar to Eq. (41), we have

$$\begin{aligned}\frac{E^s\varepsilon^2}{12}V^s + \frac{E^p\varepsilon^2}{12}V^p &= \frac{1}{2}VC_{11}\varepsilon^2\\ \frac{E^s\varepsilon_V^2}{18}V^s + \frac{E^p\varepsilon_V^2}{18}V^p &= \frac{1}{6}V(C_{11}+2C_{12})\varepsilon_V^2\end{aligned} \tag{A9}$$

Then, the moduli of the equivalent homogeneous cubic cells can be obtained from Eq. (A9) as

$$C_{11} = \frac{E^sV^s + E^pV^p}{6V},\quad C_{12} = \frac{E^sV^s + E^pV^p}{12V} \tag{A10}$$

Note that unlike the cubic cell, here $C_{12} \neq 0$, which means the existence of the overall Poisson effect in the equivalent cells.

Finally, the effective Young's modulus of the equivalent cells can be derived as

$$E = \frac{(C_{11}-C_{12})(C_{11}+2C_{12})}{C_{11}} = \frac{E^sV^s + E^pV^p}{6V} \tag{A11}$$

Modified Energy-Equivalent Method. Following the method established in Sec. 3.3, here we derive the analytical expressions of effective Young's moduli for octet and octahedral lattices with thick beams.

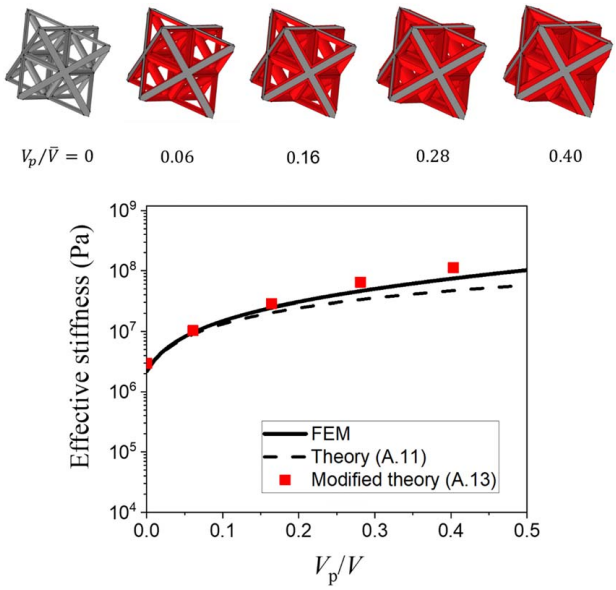

Fig. 16 Comparison between the theoretical prediction (A11), modified theoretical result (A13), and FEM simulation of the effective stiffness of the two-phase octet lattice composite with varying volume ratio V^p/V. The upper row presents the 3D images of the cell structures with $V^p/V = 0$, 0.06, 0.16, 0.28, 0.40 and the lower row displays the plot of the effective stiffness of the lattice as a function of volume ratio V^p/V. The FEM results of the specific structures in the upper row are marked with square points.

Equation (A9) can be modified as

$$\begin{aligned}\frac{t^s E^s \varepsilon^2}{8} V^s + \frac{t^p E^p \varepsilon^2}{8} V^p &= \frac{1}{2} V C_{11} \varepsilon^2 \\ \frac{E^s \varepsilon_V^2}{18} V^s + \frac{E^p \varepsilon_V^2}{18} V^p &= \frac{1}{6} V (C_{11} + 2C_{12}) \varepsilon_V^2\end{aligned} \tag{A12}$$

where t^k ($k = s, p$) is the volume ratio of the stressed region to the total region of the kth phase.

Then, the effective Young's modulus of the lattices can be obtained as

$$\begin{aligned}E &= \frac{(C_{11} - C_{12})(C_{11} + 2C_{12})}{C_{11}} \\ &= \frac{(E^s V^s + E^p V^p)[V^p E^p (9t^p - 4) + V^s E^s (9t^s - 4)]}{18V(t^s E^s V^s + t^p E^p V^p)}\end{aligned} \tag{A13}$$

It can be seen from Fig. A14 that both octet and octahedral lattices consist of tetrahedron units. Due to the complex 3D structures of octet and octahedral lattices, it is difficult to write analytical expressions of t^k ($k = s, p$) like cubic lattice (Fig. 4). Here, we make a bold assumption that the volume of the 3D stressed region of the structure is proportional to its corresponding area of 2D section, as shown in Fig. 15.

When subject to a uniaxial strain, stress occurs in four of twelve beams of the structure, with the stressed region shown in Fig. 15. The total volume of the initial solid beam is

$$V^s = \sqrt{3} l_0^2 / 4 - \left(\frac{\sqrt{3} l_0}{2} - 3R \right)^2 / \sqrt{3} \tag{A14}$$

The volume of the stressed part of the initial solid beam is

$$V^s_{strain} = \sqrt{3} l_0^2 / 4 - \left(\frac{\sqrt{3} l_0}{2} - 2R \right)^2 / \sqrt{3} \tag{A15}$$

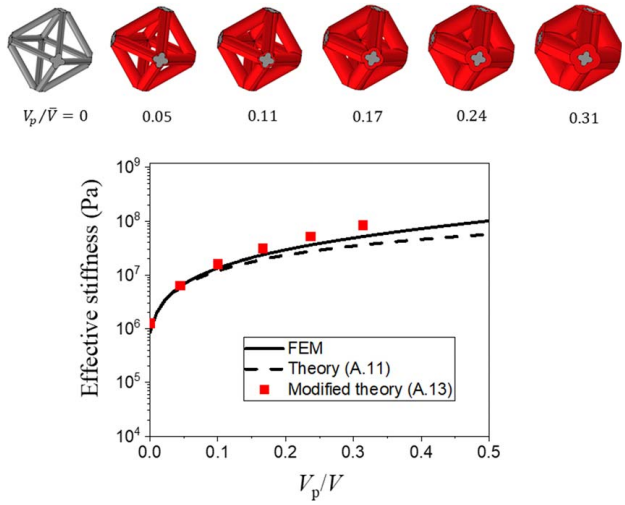

Fig. 17 Comparison between the theoretical prediction (A11), modified theoretical result (A13) and FEM simulation of the effective stiffness of the two-phase octahedral lattice composite with varying volume ratio V^p/V. The upper row presents the 3D images of the cell structures with $V^p/V = 0$, 0.05, 0.11, 0.17, 0.24, 0.31 and the lower row displays the plot of the effective stiffness of the lattice as a function of volume ratio V^p/V. The FEM results of the specific structures in the upper row are marked with square points.

The total volume of the precipitated beam is

$$V^p = \sqrt{3} l_0^2 / 4 - \left(\frac{\sqrt{3} l_0}{2} - 3R - 3H \right)^2 / \sqrt{3} - V^s \tag{A16}$$

The volume of the stressed part of the precipitated beam is

$$V^p_{strain} = V^p - \left(\frac{\sqrt{3} l_0}{2} - 3R - 2H \right)^2 / \sqrt{3} - \left(\frac{\sqrt{3} l_0}{2} - 3R - 3H \right)^2 / \sqrt{3} \tag{A17}$$

Then, the volume ratio of each phase in Eq. (A13) can be obtained once the initial structure is given, as

$$t^s = \frac{V^s_{strain}}{V^s}, \quad t^p = \frac{V^p_{strain}}{V^p} \tag{A18}$$

The effective Young's modulus can be obtained using Eq. (A13). For the case that the beams are thin sufficiently, we have $t^s = t^p = 2/3$. Then, Eq. (A13) reduces to the formulation (A11).

We verify the accuracy of the theoretical prediction Eq. (A11) and modified theoretical model Eq. (A13) for the overall stiffness of the growing two-phase octet and octahedral lattice cells in Figs. 16 and 17, respectively. The initial volume ratio of the solid frame of the octet cell is $V^s/V = 10\%$ and that of the octahedral cell is $V^s/V = 4\%$. Good agreement between the theoretical prediction and FEM simulation is presented, indicating the validity of Eqs. (A11) and (A13). Moreover, our modified theoretical model shows a better prediction result for thick-beam structures.

References

[1] Noor, A. K., 1988, "Continuum Modeling for Repetitive Lattice Structures," ASME Appl. Mech. Rev., **41**(7), pp. 285–296.

[2] Vasiliev, V. V., Barynin, V. A., and Rasin, A. F., 2001, "Anisogrid Lattice Structures–Survey of Development and Application," Compos. Struct., **54**(2–3), pp. 361–370.

[3] Kossevich, A. M., 1999, *The Crystal Lattice: Phonons, Solitons, Dislocations*, Wiley-VCH, Berlin.

[4] Trubin, A., 2015, *Lattices of Dielectric Resonators*, Vol. 53, Springer, New York.

[5] Fan, H. L., Yang, W., Wang, B., Yan, Y., Fu, Q., Fang, D. N., and Zhuang, Z., 2006, "Design and Manufacturing of a Composite Lattice Structure Reinforced by Continuous Carbon Fibers," Tsinghua Sci. Technol., **11**(5), pp. 515–522.

[6] Xiong, J., Ma, L., Wu, L., Wang, B., and Vaziri, A., 2010, "Fabrication and Crushing Behavior of Low Density Carbon Fiber Composite Pyramidal Truss Structures," Compos. Struct., **92**(11), pp. 2695–2702.

[7] Vasiliev, V. V., Barynin, V. A., and Razin, A. F., 2012, "Anisogrid Composite Lattice Structures–Development and Aerospace Applications," Compos. Struct., **94**(3), pp. 1117–1127.

[8] George, T., 2014, "Carbon Fiber Composite Cellular Structures," Dissertation, University of Virginia, Charlottesville, VA.

[9] Zhang, Y., Ha, S., Sharp, K., Guest, J. K., Weihs, T. P., and Hemker, K. J., 2015, "Fabrication and Mechanical Characterization of 3D Woven Cu Lattice Materials," Mater. Des., **85**, pp. 743–751.

[10] Jiang, S., Sun, F., Zhang, X., and Fan, H., 2017, "Interlocking Orthogrid: an Efficient Way to Construct Lightweight Lattice-Core Sandwich Composite Structure," Compos. Struct., **176**, pp. 55–71.

[11] Xu, B., Yin, S., Wang, Y., Li, H., Zhang, B., and Ritchie, R. O., 2017, "Long-Fiber Reinforced Thermoplastic Composite Lattice Structures: Fabrication and Compressive Properties," Compos. Part A, **97**, pp. 41–50.

[12] Fan, H. L., Zeng, T., Fang, D. N., and Yang, W., 2010, "Mechanics of Advanced Fiber Reinforced Lattice Composites," Acta Mech. Sin., **26**(6), pp. 825–835.

[13] Maconachie, T., Leary, M., Lozanovski, B., Zhang, X., Qian, M., Faruque, O., and Brandt, M., 2019, "SLM Lattice Structures: Properties, Performance, Applications and Challenges," Mater. Des., **183**, 108137.

[14] Li, B., Li, Z., Zhou, J., Ye, L., and Li, E., 2015, "Damage Localization in Composite Lattice Truss Core Sandwich Structures Based on Vibration Characteristics," Compos. Struct., **126**, pp. 34–51.

[15] Voyiadjis, G. Z., 2015, *Handbook of Damage Mechanics: Nano to Macro Scale for Materials and Structures*, Springer, New York.

[16] Gibson, L. J., Ashby, M. F., and Harley, B. A., 2010, *Cellular Materials in Nature and Medicine*, Cambridge University Press, Cambridge.

[17] Hu, Z., Gadipudi, V. K., and Salem, D. R., 2019, "Topology Optimization of Lightweight Lattice Structural Composites Inspired by Cuttlefish Bone," Appl. Compos. Mater., **26**(1), pp. 15–27.

[18] Huang, W., Restrepo, D., Jung, J. Y., Su, F. Y., Liu, Z., Ritchie, R. O., McKittrick, J., Zavattieri, P., and Kisailus, D., 2019, "Multiscale Toughening Mechanisms in Biological Materials and Bioinspired Designs," Adv. Mater., **31**(43), p. 1901561.

[19] da Costa Reis, J., and Oliveira, M. T., 2020, "Bone: Functions, Structure and Physiology," *The Computational Mechanics of Bone Tissue*, J. Belinha, M. C. Manzanares-Céspedes, and A. M. G. Completo, eds., Springer, Cham, pp. 3–43.

[20] Pan, C., Han, Y., and Lu, J., 2020, "Design and Optimization of Lattice Structures: A Review," Appl. Sci., **10**(18), p. 6374.

[21] Fan, H. L., and Yang, W., 2006, "An Equivalent Continuum Method of Lattice Structures," Acta Mech. Solida Sin., **19**(2), pp. 103–113.

[22] Hawreliak, J. A., Lind, J., Maddox, B., Barham, M., Messner, M., Barton, N., Jensen, B. J., and Kumar, M., 2016, "Dynamic Behavior of Engineered Lattice Materials," Sci. Rep., **6**(1), pp. 1–7.

[23] Song, J., Gao, L., Cao, K., Zhang, H., Xu, S., Jiang, C., Surjadi, J. U., Xu, Y., and Lu, Y., 2018, "Metal-Coated Hybrid Meso-Lattice Composites and Their Mechanical Characterizations," Compos. Struct., **203**, pp. 750–763.

[24] Wang, B., Wu, L., Ma, L., Sun, Y., and Du, S., 2010, "Mechanical Behavior of the Sandwich Structures With Carbon Fiber-Reinforced Pyramidal Lattice Truss Core," Mater. Des., **31**(5), pp. 2659–2663.

[25] Li, W., Sun, F., Wang, P., Fan, H., and Fang, D., 2016, "A Novel Carbon Fiber Reinforced Lattice Truss Sandwich Cylinder: Fabrication and Experiments," Compos. Part A, **81**, pp. 313–322.

[26] Frulloni, E., Kenny, J. M., Conti, P., and Torre, L., 2007, "Experimental Study and Finite Element Analysis of the Elastic Instability of Composite Lattice Structures for Aeronautic Applications," Compos. Struct., **78**(4), pp. 519–528.

[27] Morozov, E. V., Lopatin, A. V., and Nesterov, V. A., 2011, "Finite-Element Modelling and Buckling Analysis of Anisogrid Composite Lattice Cylindrical Shells," Compos. Struct., **93**(2), pp. 308–323.

[28] Hong, W., Zhao, X., Zhou, J., and Suo, Z., 2008, "A Theory of Coupled Diffusion and Large Deformation in Polymeric Gels," J. Mech. Phys. Solids, **56**(5), pp. 1779–1793.

[29] Liu, Z., Swaddiwudhipong, S., and Hong, W., 2013, "Pattern Formation in Plants via Instability Theory of Hydrogels," Soft Matter, **9**(2), pp. 577–587.

[30] Balbi, V., Kuhl, E., and Ciarletta, P., 2015, "Morphoelastic Control of Gastro-Intestinal Organogenesis: Theoretical Predictions and Numerical Insights," J. Mech. Phys. Solids, **78**, pp. 493–510.

[31] Du, Y., Su, Y., Lü, C., Chen, W., and Destrade, M., 2020, "Electro-Mechanically Guided Growth and Patterns," J. Mech. Phys. Solids, **143**, 104073.

[32] Compton, B. G., and Lewis, J. A., 2014, "3D-Printing of Lightweight Cellular Composites," Adv. Mater., **26**(34), pp. 5930–5935.

[33] Wang, Q. M., Jackson, J. A., Ge, Q., Hopkins, J. B., Spadaccini, C. M., and Fang, N. X., 2016, "Lightweight Mechanical Metamaterials With Tunable Negative Thermal Expansion," Phys. Rev. Lett., **117**(17), p. 175901.

[34] Liu, S., Li, Y., and Li, N., 2018, "A Novel Free-Hanging 3D Printing Method for Continuous Carbon Fiber Reinforced Thermoplastic Lattice Truss Core Structures," Mater. Des., **137**, pp. 235–244.

[35] Yu, K. H., Du, H. X., Xin, A., Lee, K. H., Feng, Z., Masri, S. F., Chen, Y., Huang, G. L., and Wang, Q. M., 2020, "Healable, Memorizable, and Transformable Lattice Structures Made of Stiff Polymers," NPG Asia Mater., **12**(1), pp. 1–16.

[36] Yu, K. H., Xin, A., Du, H. X., Li, Y., and Wang, Q. M., 2019, "Additive Manufacturing of Self-Healing Elastomers," NPG Asia Mater., **11**(1), pp. 1–11.

[37] Chen, L. Q., 2002, "Phase-Field Models for Microstructure Evolution," Annu. Rev. Mater. Res., **32**(1), pp. 113–140.

[38] Provatas, N., and Elder, K., 2011, *Phase-Field Methods in Materials Science and Engineering*, John Wiley & Sons, Hoboken, NJ.

[39] Berger, J. B., Wadley, H. N. G., and McMeeking, R. M., 2017, "Mechanical Metamaterials at the Theoretical Limit of Isotropic Elastic Stiffness," Nature, **543**(7646), pp. 533–537.

[40] Xin, A., Du, H., Yu, K., and Wang, Q., 2020, "Mechanics of Bacteria-Assisted Extrinsic Healing," J. Mech. Phys. Solids, **139**, 103938.

[41] She, M., 2008, "Phase Field Model for Precipitates in Crystals," Doctoral dissertation, Massachusetts Institute of Technology, Cambridge, MA.

[42] Porter, D. A., and Easterling, K. E., 2009, *Phase Transformations in Metals and Alloys (Revised Reprint)*, CRC Press, Boca Raton, FL.

[43] Cahn, J. W., and Allen, S. M., 1977, "A Microscopic Theory for Domain Wall Motion and Its Experimental Verification in Fe-Al Alloy Domain Growth Kinetics," Le J. Phys. Colloques, **38**(C7), pp. C7–51.

[44] Ratke, L., and Voorhees, P. W., 2002, "Transport of Heat and Mass," *Growth and Coarsening*. Springer, Berlin, Heidelberg, pp. 43–55.

[45] Zener, C., 1949, "Theory of Growth of Spherical Precipitates From Solid Solution," J. Appl. Phys., **20**(10), pp. 950–953.

[46] Su, Y. P., Wang, H. M., Zhang, C. L., and Chen, W. Q., 2016, "Propagation of Non-Axisymmetric Waves in an Infinite Soft Electroactive Hollow Cylinder Under Uniform Biasing Fields," Int. J. Solids Struct., **81**, pp. 262–273.

[47] Balluffi, R. W., Allen, S. M., and Carter, W. C., 2005, *Kinetics of Materials*, John Wiley & Sons, Hoboken, NJ.

[48] Wheeler, A. A., Boettinger, W. J., and McFadden, G. B., 1992, "Phase-Field Model for Isothermal Phase Transitions in Binary Alloys," Phys. Rev. A, **45**(10), pp. 7424–7439.

[49] Ogden, R. W., 1997, *Non-Linear Elastic Deformations*, Courier Corporation, Chelmsford, MA.